Active acoustic switches using two-dimensional granular crystals

Qikai Wu,[1] Chunyang Cui,[2] Thibault Bertrand,[3,1] Mark D. Shattuck,[4,1] and Corey S. O'Hern[1,5,6]

[1]*Department of Mechanical Engineering and Materials Science, Yale University, New Haven, Connecticut 06520, USA*
[2]*State Key Laboratory of Hydroscience and Engineering, Tsinghua University, 100084 Beijing, China*
[3]*Department of Mathematics, Imperial College London, South Kensington Campus, London SW7 2AZ, England, United Kingdom*
[4]*Department of Physics and Benjamin Levich Institute, The City College of the City University of New York, New York, 10031, USA*
[5]*Department of Physics, Yale University, New Haven, Connecticut 06520, USA*
[6]*Department of Applied Physics, Yale University, New Haven, Connecticut 06520, USA*

We employ numerical simulations to study active transistor-like switches made from two-dimensional (2D) granular crystals containing two types of grains with the same size but different masses. We tune the mass contrast and arrangement of the grains to maximize the width of the frequency band gap in the device. The input signal is applied to a single grain on one side of the device, and the output signal is measured from another grain on the other side of the device. Changing the size of one or many grains tunes the pressure, which controls the vibrational response of the device. Switching between the on and off states is achieved using two mechanisms: (1) pressure-induced switching where the interparticle contact network is the same in the on and off states and (2) switching through contact breaking. In general, the performance of the acoustic switch, as captured by the gain ratio and switching time between the on and off states, is better for pressure-induced switching. We show that in these acoustic switches the gain ratio between the on and off states can be larger than 10^4 and the switching time (multiplied by the driving frequency) is comparable to that obtained recently for sonic crystals and less than that for photonic transistor-like switches. Since the self-assembly of grains with different masses into 2D granular crystals is challenging, we describe simulations of circular grains with small circular knobs placed symmetrically around the perimeter mixed with circular grains without knobs. Using umbrella sampling techniques, we show that grains with six knobs most efficiently form the hexagonal crystals that yield the largest frequency band gap. Using the simulation results, we estimate the time required for vibration experiments to generate granular crystals of millimeter-sized steel beads with maximal band gaps.

I. INTRODUCTION

A number of recent studies have demonstrated the potential for granular crystals to serve as switches [1], rectifiers [2], and other logic elements [3] in circuits that use mechanical rather than electrical signals. These mechanical devices have potential applications in vibration isolation [4], acoustic cloaks [5], and one-way sound propagation [6]. Many prior studies have used one-dimensional (1D) granular chains as model systems [7,8] and relied on the nonlinear Hertzian interparticle contact law to tailor the acoustic response [9–11]. For example in Ref. [3], researchers developed an acoustic switch by taking advantage of the fact that 1D granular chains composed of steel beads possess a high-frequency cutoff $\omega_{\max}$, beyond which an input signal cannot propagate. Thus, when the system is driven at $\omega_0 > \omega_{\max}$, the response is extremely small, i.e., it exists in the "off" state. However, when the system is also driven at frequency $\omega_c < \omega_{\max}$, nonlinearities from the Hertzian interactions between grains can induce a strong response at ω_0 (i.e., produce an "on" state), as well as linear combinations of ω_0 and ω_c. The authors showed that the amplitude of the response at ω_0 in the on state was 3.5 orders of magnitude larger than that of the off state [3]. This seminal work demonstrated the ability to actively control mechanical signal propagation in 1D granular chains.

Transistors are fundamental components of modern electrical devices that perform logic operations by amplifying or switching electrical signals [12]. In this study, we numerically design a transistor-like acoustic switch using 2D granular crystals composed of grains with two different masses m_L and m_S. In a typical field-effect transistor, the drain-to-source current is controlled by the voltage applied between the gate and source terminals. Analogously, in our system, the mechanical response will be controlled by the applied pressure. As shown in Fig. 1, we will consider three-port devices. We will send mechanical signals to a single particle (port 3) on one side of the system, apply pressure by changing the size of a single or many grains (port 2), and measure the power spectrum of the displacements of another grain on the other side of the system (port 1).

Granular crystals composed of two types of grains with the same size, but with mass contrast $m_L/m_S > 1$, possess band gaps in their vibrational density of states [8,13]. The width of the band gap depends strongly on pressure [14]. Thus, by varying the pressure at fixed driving frequency, we can change the range of the frequency band gap so that the driving frequency occurs within or outside the band gap. When the system is excited at a frequency within the band gap, the signal will not propagate and the switch is off. When the system is excited at a frequency outside the band gap, it will propagate
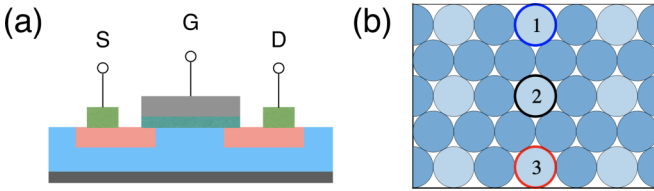
FIG. 1. (a) A schematic of a metal-oxide-semiconductor field-effect transistor (MOSFET) with gate (G), source (S), and drain (D) ports and (b) a schematic of a switch made from a 2D granular crystal with three ports for the (1) output, (2) control, and (3) input signals.

and the switch is on. Thus, by changing the pressure, we can actively switch the device between the off and on states. In addition, using 2D granular crystals allows us to determine the effects of the polarization of the mechanical signal and contact breaking [15,16], where grains come in and out of contact during vibration, on the performance of acoustic switches.

We will quantify the performance of the acoustic switch by measuring its gain, which is the ratio of the amplitude of the displacement spectrum at the driving frequency for the output versus that of the input particle (via ports 1 and 3). We find that the ratio of the gain for the on and off states of the device can be four orders of magnitude or larger. We also characterize the time required to switch between the on and off states and vice versa. We find that there is a trade-off between the switching time and gain ratio. We achieve the fastest switching times for devices with the smallest gain ratios between the on and off states. In addition, we investigated the effect of contact breaking on the performance of granular acoustic switches. We find that when changes in pressure cause contact breaking in the device, the performance of the switch is degraded. In particular, devices with contact breaking can only achieve modest gain ratios, where the gain for the on state is 1.5 orders of magnitude larger than that for the off state. We also studied the performance of the acoustic switch when we adjust the sizes of a single versus multiple grains to induce changes in pressure. Adjusting the sizes of multiple grains allows the device to achieve larger gain ratios. In addition, since it is typically difficult to generate 2D granular crystals containing grains with different masses in both simulations and experiments [17,18], we also describe a method to generate granular crystals in 2D using circular grains that include small circular knobs on their surfaces. We employ discrete element method simulations with advanced sampling techniques to determine the number and placement of the knobs that yield the most efficient 2D crystallization. We then estimate the time required to achieve crystallized configurations in vibration experiments on granular materials.

This article includes three additional sections and two Appendices. In Methods, we describe calculations of the vibrational density of states for 2D granular crystals composed of two types of grains with the same size, but with mass contrast $m_L/m_S > 1$. We measure the width of the frequency band gap as a function of the mass contrast, arrangement of the heavy and light grains, and pressure. In addition, we describe the input signal, how the output signal will be measured, and the methods that will be used to change the pressure in the device. In Results, we show our calculations of the gain ratios for

the on and off states in devices where the pressure is varied and in regimes where the network of interparticle contacts is fixed or fluctuates. We provide results for the gain ratios for systems in steady state and study the gain as a function of time after the device switches from on to off and vice versa. We also describe discrete element method simulations coupled with advanced sampling methods in 2D of circular grains containing small circular knobs on their surfaces and identify the number and placement of knobs that give rise to the most efficient crystallization. From the probabilities of achieving crystalline configurations in the simulations, we estimate the time required to generate the crystalline configurations in vibration experiments of typical granular materials. In the final section, we summarize our most important results, suggest future calculations, and discuss the possibility to build mechanical circuits that can perform logical operations. The two Appendices provide additional technical details that support the methods and results in the main text. In Appendix A, we show that the numerical methods used to calculate the discrete Fourier transform of the input and output signals do not affect our results. In Appendix B, we show results for the performance of 2D granular acoustic switches with small band gaps.

II. METHODS

To narrow the parameter space, we focus on 2D granular systems composed of frictionless circular disks in the absence of gravity. For most studies, the systems include two types of disks with the same diameter σ, but different masses, m_L and m_S, with $m_L > m_S$. The $N = N_L + N_S$ disks (where N_L and N_S are the numbers of disks with mass m_L and m_S, respectively) interact via the pairwise, purely repulsive linear spring potential,

$$U(r_{ij}) = \frac{\epsilon}{2}\left(1 - \frac{r_{ij}}{\sigma}\right)^2 \Theta\left(1 - \frac{r_{ij}}{\sigma}\right), \quad (1)$$

where r_{ij} is the separation between the centers of disks i and j, ϵ is the energy scale of the repulsive interaction, and $\Theta(x)$ is the Heaviside step function that sets $U(r_{ij}) = 0$ when the disks are not in contact with $r_{ij} > \sigma_{ij}$. For most studies, the simulation cell is rectangular with area $A = L_x L_y$ and dimensions $L_x = N_x \sigma$, and $L_y = N_y \sqrt{3}\sigma/2$, where $N = N_x N_y$, and N_x and N_y are the number of particles in the x and y directions, so that it can accommodate a hexagonal lattice. We implement periodic boundary conditions in the x direction, and fixed, flat boundaries in the y direction. Interactions between a circular grain and the wall are implemented by assuming that a ghost particle is placed at a symmetric position behind the wall. We focus on systems with relatively small N, from $N = 30$ to 100 grains, since it is difficult to self-assemble perfect crystalline structures in large systems [17,18]. Below, lengths, energies, stresses, and frequencies will be given in units of σ, ϵ, ϵ/σ^2, and $\sqrt{\epsilon/m_S\sigma^2}$, respectively.

Most of the systems we consider are mechanically stable with a full spectrum of $2N$ nonzero vibrational frequencies, ω_k, with $k = 1, \ldots, 2N$. The vibrational frequencies are obtained by calculating the eigenvalues $\lambda_k = \omega_k^2$ of the mass-weighted dynamical matrix [19] $\mathcal{M}_{kj} = M_{ki}^{-1}H_{ij}$, where $H_{ij} = \partial^2 U/\partial\xi_i\partial\xi_j$ is the Hessian of the total potential energy
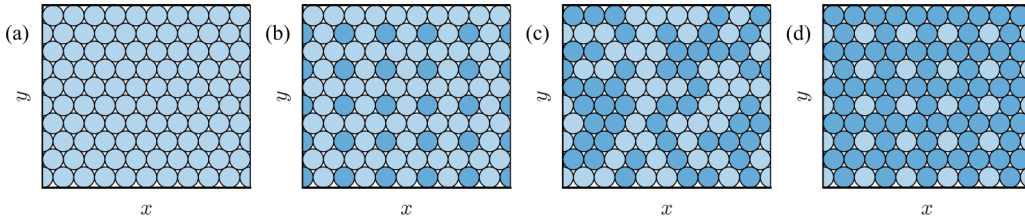
FIG. 2. Mechanically stable packings of $N = 100$ disks with the same size, two different masses, and mass ratio $m_L/m_S = 10$ arranged on a hexagonal lattice with periodic and fixed boundary conditions in the x and y directions, respectively. In (a), the system is homogeneous with $N_L = 0$ (dark blue) and $N_S = N$ (light blue). In (b), we set $N_L = 25$ and $N_S = 75$. The first row contains all small masses. In the second row, the large and small masses alternate. The third row alternates between large and small masses, and this order repeats for a total of 10 rows. In (c), $N_L = 50$ and $N_S = 50$ and large and small masses are distributed randomly on the hexagonal lattice. Panel (d) is similar to (b) except inverted with $N_L = 75$ and $N_S = 25$.

$U = \sum_{i>j} U(r_{ij})$, $\xi_i = x_i$, y_i, and $M_{ij} = m_{L,S}\delta_{ij}$ is the diagonal mass matrix. We also determine the eigenvectors $\vec{\lambda}^k$ that correspond to each eigenfrequency ω_k with $\vec{\lambda}^k \cdot \vec{\lambda}^k = 1$, where $\vec{\lambda}^k = \{x_1^k, y_1^k, \ldots, x_N^k, y_N^k\}$.

We calculate the eigenfrequency spectrum of the mass-weighted dynamical matrix for several arrangements of the large and small masses on a hexagonal lattice with $N = 100$ shown in Fig. 2. We illustrate in Fig. 3 that for a hexagonal lattice with a uniform mass distribution [Fig. 2(a)], the frequency spectrum is nearly continuous with a high-frequency cutoff $\omega_{\max} \approx 25$. For mixtures of large and small masses with a mass ratio $m_L/m_S = 10$ [Figs. 2(b) and 2(c)], a small frequency band gap develops in the range $5 \lesssim \omega \lesssim 8$. For each eigenfrequency spectrum, we identify the maximum frequency difference $w = \max_k(\omega_{k+1} - \omega_k)$.

We find that the arrangement of large and small masses that gives rise to the largest band gap w is the alternating pattern in Fig. 2(d). In Fig. 4, we show that for the optimal arrangement of large and small masses [i.e., Fig. 2(d)], w increases with m_L/m_S, reaching a plateau of $w \approx 16$ in the

$m_L/m_S \to \infty$ limit. For most of our studies, we use a mass ratio, $m_L/m_S = 10$, with $w \approx 10$.

The width of the frequency band gap can also be tuned by changing the pressure of the system. When all of the disks are at contact and placed on a hexagonal lattice, the packing fraction is $\phi_{\text{xtal}} = \pi/2\sqrt{3} \approx 0.91$ for systems with periodic boundary conditions in both the x and y directions (and ≈ 0.89 for systems with fixed boundaries in the y direction and periodic boundaries in the x direction), and the pressure $p = A^{-1}\sum_{i>j} \vec{f}_{ij} \cdot \vec{r}_{ij}/2$ is nearly zero, where $\vec{f}_{ij} = -dU/d\vec{r}_{ij}$ is the repulsive force on disk i arising from disk j. We can change the pressure of the system by increasing or decreasing the diameter of the disks by an increment in packing fraction $\Delta\sigma/\sigma = \Delta\phi/\phi$ or equivalently by bringing the fixed walls in the y direction closer together or further apart. We define the packing fraction as $\phi = A^{-1}\sum_{i=1}^{N} \pi\sigma_i^2/4$, even for systems in which the grains overlap. In Fig. 5(a), we show the spectrum of eigenfrequencies of the mass-weighted dynamical matrix for the configuration in Fig. 2(d) with $m_L/m_S = 10$ at low $p = 10^{-3}$ and high pressure $p = 1$. For the system at low pressure, we can set the driving frequency at $\omega_0 \approx 9$ in the band gap,
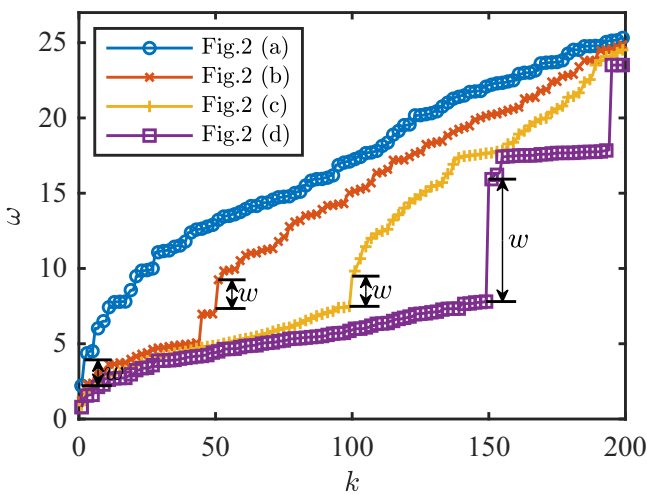

FIG. 3. Eigenfrequencies of the mass-weighted dynamical matrix ω_k, sorted in ascending order and indexed by k, for the $N = 100$ configurations in Fig. 2. (a) Circles, (b) Xs, (c) plusses, and (d) squares with periodic and fixed boundary conditions in the x and y directions, respectively. w indicates the maximum band gap in the eigenfrequency spectrum.
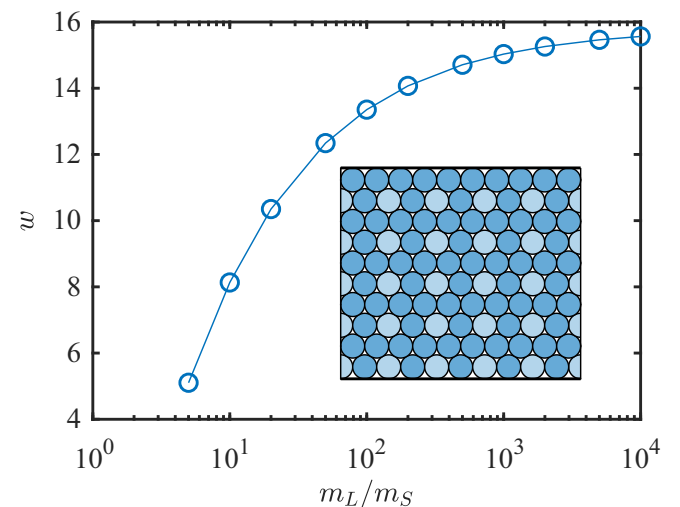

FIG. 4. The width w of the maximum band gap in the eigenfrequency spectrum of the mass-weighted dynamical matrix for the configuration in Fig. 2(d) (and inset) as a function of the mass ratio m_L/m_S.
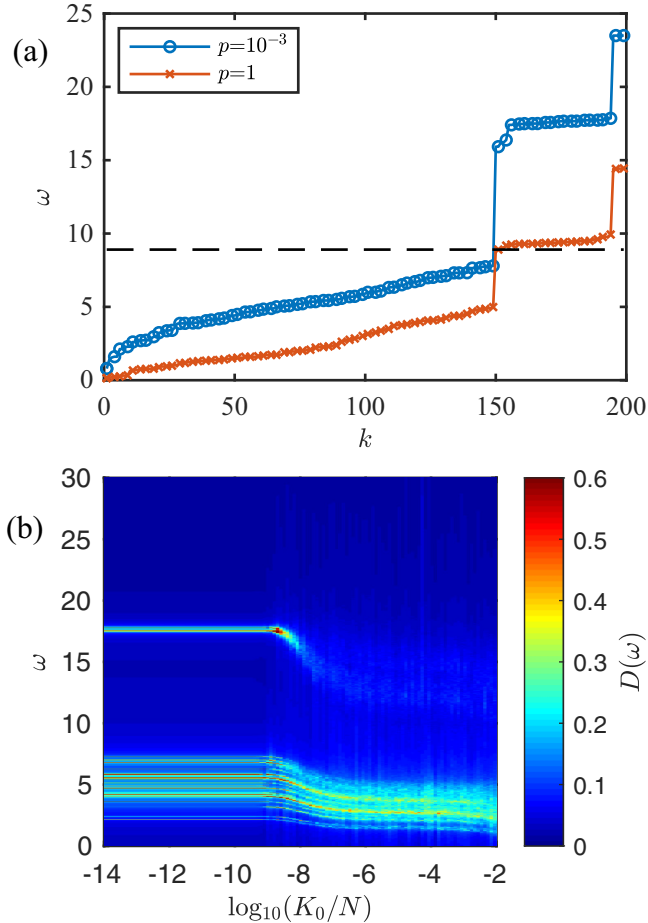
FIG. 5. (a) Spectrum of eigenfrequencies of the mass-weighted dynamical matrix sorted in ascending order with index k for systems with $N = 100$ disks, $m_L/m_S = 10$, and arranged on a hexagonal lattice in the optimal configuration in Fig. 2(d) at pressure $p = 10^{-3}$ (circles) and 1 (Xs). The dashed line indicates a driving frequency at which the acoustic switch can operate. (b) The Fourier transform of the velocity correlation function $D(\omega)$ for the mechanically stable packing in Fig. 2(d) at pressure $p = 10^{-4}$ after adding velocities to all grains such that the eigenfrequencies of the mass-weighted dynamical matrix are included with equipartition of the total kinetic energy K_0. The color scale from dark red to violet represents decreasing $D(\omega)$ on a linear scale.

and the system exists in the off state. When we compress the system to high pressure, all of the eigenfrequencies decrease, and the width of the band gap also decreases. At high pressure, the driving frequency is no longer in the band gap, and the system exists in the on state. Thus, 2D granular crystals can be switched from on to off and vice versa by changing the pressure.

Contact breaking, a significant source of nonlinearity in granular materials [16,20,21], can also be used to switch between the on and off states and vice versa in 2D granular crystals. Contact breaking occurs when the system is driven at sufficiently large amplitudes (e.g., through vibration or shear) so that the network of interparticle contacts changes. The characteristic driving amplitude at which contact breaking occurs decreases with pressure. When the system can break

interparticle contacts and form new ones, the frequencies of strong peaks in the Fourier transform of the velocity autocorrelation function of the disks will differ from the spectrum of eigenfrequencies of the mass-weighted dynamical matrix.

To illustrate contact breaking and its effect on the vibrational response, we excite a 2D granular crystal by setting the velocities of the grains such that all eigenmodes of the mass-weighted dynamical matrix are included with equipartition of the total kinetic energy, K_0. To determine the vibrational response, we calculate the Fourier transform of the normalized velocity autocorrelation function,

$$D(\omega) = \int_0^\infty dt \frac{\langle \vec{v}(t_0 + t) \cdot \vec{v}(t_0) \rangle}{\langle \vec{v}(t_0) \cdot \vec{v}(t_0) \rangle} e^{i\omega t}, \qquad (2)$$

where $\langle . \rangle$ indicates an average over all of the disks and time origins t_0. In Fig. 5(b), we show $D(\omega)$ as a function of K_0/N for the optimal configuration in Fig. 2(d) at $p = 10^{-4}$. At small vibration amplitudes, $D(\omega)$ is large at all of the $2N$ eigenfrequencies of the mass-weighted dynamical matrix. When the vibration amplitude exceeds $K_0/N \approx 10^{-9}$ existing contacts begin to break and new contacts begin to form, $D(\omega)$ broadens and spreads to lower frequencies. In particular, for amplitudes above 10^{-9}, there is a very weak response at high frequencies. Thus, contact breaking can also be used to switch between the on and off states. For example, when the system is driven at $\omega_0 = 18$ at small K_0/N, the switch is on. However, when the system is driven at the same ω_0 with amplitude $K_0/N \gtrsim 10^{-9}$, the switch is off.

For the specific device geometry, we consider a three-port switch built from the 2D granular crystal shown in Fig. 6. We will add sinusoidal displacements with amplitude A_0 at driving frequency ω_0 to a single disk on the bottom wall (port 3),

$$x_3(t) = x_3^0 + A_0 \sin(\omega_0 t), \qquad (3)$$

where x_3^0 is the position of disk 3 in the mechanically stable packing. When we add a continuous input signal, we also include a viscous damping force for each disk i, $\vec{F}_i = -b\vec{v}_i$, where b is the damping coefficient. After the system reaches a steady state, we determine the response of the system by measuring the Fourier transform of the x displacement of disk 1 that is several layers away from disk 3 in the top wall (port 1): $F_1(\omega) = \int_0^\infty [x_1(t) - x_1^0] e^{i\omega t} dt$. The Fourier transform is calculated numerically as discussed in Appendix A. The gain of the system is defined as the ratio of the response at the output port 1 to strength of the signal at the input port 3 at the driving frequency ω_0:

$$G(\omega_0) = \frac{F_1(\omega_0)}{F_3(\omega_0)}. \qquad (4)$$

Note that we chose the input and output signals to be in the x direction, which we assume has a significant overlap with the eigenmodes of the system. We deliberately did not consider input and output signals along eigenmodes since they are difficult to measure experimentally in 2D granular media.

We will actively control the response of the device (i.e., through port 2) by varying the pressure in the device. We will adjust the pressure by changing the size of grain i: $\Delta_i(t) = (\sigma_i(t) - \sigma)/\sigma$, where σ is the unperturbed diameter of the grains. For the control signal, we can also vary the fraction of grains f whose sizes are changed by Δ. Below, we will
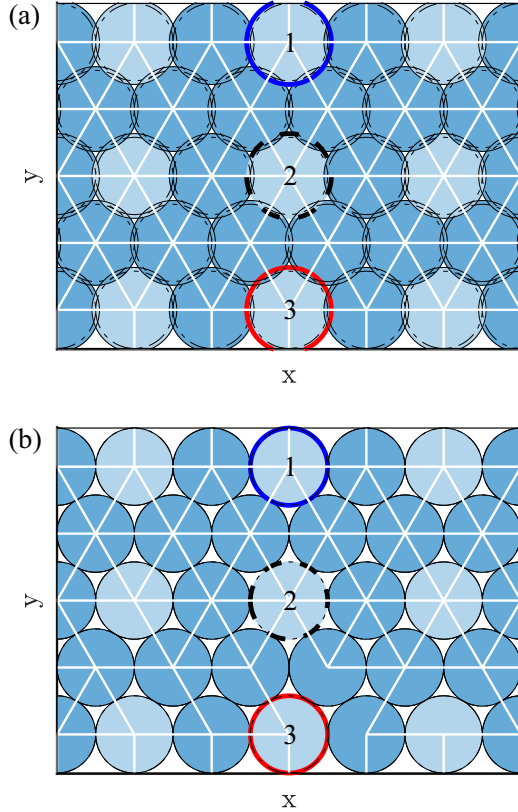
FIG. 6. (a) An illustration of a three port acoustic switch with fixed, flat boundary conditions in the y direction and periodic boundary conditions in the x direction. The device includes $N = 30$ disks (with $N_L = 21$ (dark), $N_S = 9$ (light), and $m_L/m_S = 10$) arranged on a hexagonal lattice. The solid white lines indicate the $N_c = 90$ distinct contacts between disks. Disk 3 is the input port, indicating where the system will be driven. The gain of the system is measured via the output port, labeled disk 1. The switch can be turned on and off by varying the pressure of the system through port 2, e.g., by changing the size of a single disk or all disks in the system. Here, the device changes from pressure $p = 10^{-6}$ (dashed outline) to 10^{-1} (solid outline) when all disks increase in size. (b) Illustration of the device in (a) at $p = 10^{-6}$ with disk 3 driven at $A_0 = 10^{-6}$ and frequency $\omega_0 = 16.0$, which causes contact breaking. In this snapshot, the device has four fewer contacts than in (a). The central grain with the dashed outline provides the pressure control when we use single-particle control for port 2.

consider the extremes $f = 1/N$ (one grain) and 1 (all grains). The case $f = 1$ is depicted in Fig. 6(a).

III. RESULTS

We describe the results on acoustic switches constructed from 2D granular crystals in four subsections. In Sec. III A, we focus on acoustic devices that can switch between the on and off states by changing the size of all particles in the system to control the pressure, and both the on and off states have the same network of interparticle contacts. These devices can achieve large gain ratios of at least four orders of magnitude between the on and off states. However, the switching times are rather large, exceeding hundreds of oscillations of the driving frequency. Further, there is a trade-off between gain
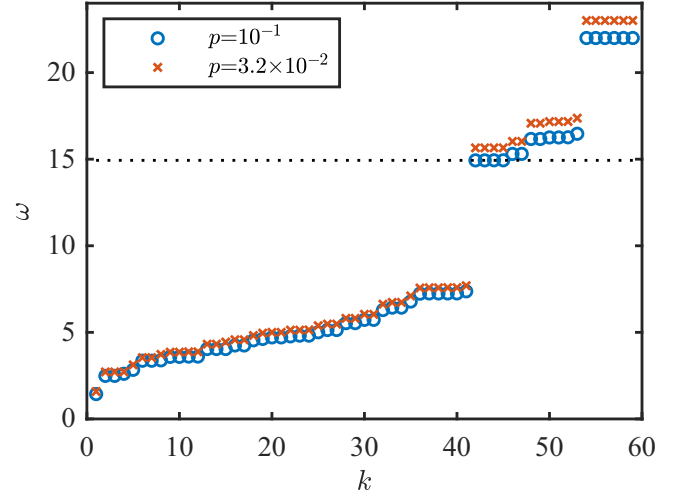

FIG. 7. The eigenfrequencies of the mass-weighted dynamical matrix plotted in increasing order with index k for the acoustic device in Fig. 6 at pressure $p = 10^{-1}$ (the "on" state, circles) and 3.2×10^{-2} (the "off" state, ✕s). The horizontal line at $\omega = 14.9$ indicates a potential driving frequency that yields a large gain ratio between the on and off states.

ratios and switching times, i.e., the largest gain ratios are achieved for the slowest switching times. In Sec. III B, we discuss acoustic devices in which contact breaking occurs, i.e., the on and off states possess different interparticle contact networks. In general, these devices have worse performance (smaller gain ratios) than those for which the interparticle contact networks are the same in the on and off states. However, switching between the on and off states in these devices can be achieved at much lower pressures. In Sec. III C, we discuss the pressure operating regime for the acoustic device when the size of only a single control particle is used to tune between the on and off states. In general, devices with a single control particle possess smaller gain ratios than those with many control particles. In Sec. III D, we describe a novel simulation technique, where we add small circular knobs to the surface of circular grains, that can robustly generate the ordered disk packing with the optimal arrangement of more and less massive grains in Fig. 2(d). A similar technique can be used in experiments to generate 2D granular crystals.

A. Pressure-induced switching

In Fig. 7, we show the eigenfrequencies of the mass-weighted dynamical matrix for the device in Fig. 6(a) in the high-pressure regime, $p = 10^{-1}$ and 3.2×10^{-2}. Changes in the pressure of the device allow us to tune the frequency range of the band gap. When we drive the system at $\omega_0 = 14.9$ with $p = 10^{-1}$, we expect the gain to be large since the density of states has weight at the driving frequency. In contrast, when we drive the system at the same frequency and $p = 3.2 \times 10^{-2}$, there is no weight in the density of states at the driving frequency and we expect the gain be much smaller, even though the interparticle contact network is the same as that for the device at $p = 10^{-1}$.

In Fig. 8(a), we show the Fourier transform $F_1(\omega)$ of the x displacement of the output disk 1 in the device after
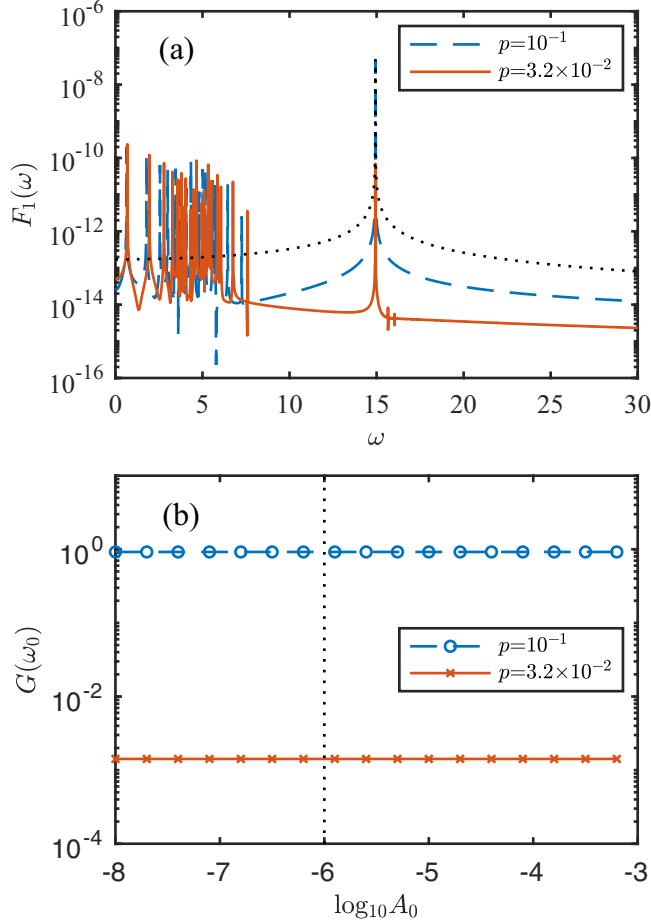
FIG. 8. (a) The Fourier transform $F_1(\omega)$ of the x displacement of disk 1 for the acoustic device with pressure $p = 10^{-1}$ (dashed line) and 3.2×10^{-2} (solid line) obtained by driving disk 3 sinusoidally with amplitude $A_0 = 10^{-6}$ and frequency $\omega_0 = 14.9$. The dotted line shows the Fourier transform $F_3(\omega)$ of the x displacement of the input disk 3. (b) The gain G(ω_0) [defined in Eq. (4)] plotted as a function of the driving amplitude A_0 with driving frequency $\omega_0 = 14.9$ for the device at pressure $p = 10^{-1}$ (open circles) and 3.2×10^{-2} (Xs).

driving the input disk 3 sinusoidally according to Eq. (3) with amplitude $A_0 = 10^{-6}$ and frequency $\omega_0 = 14.9$. Since displacing disk 3 in the x direction is not a pure eigenmode of the mass-weighted dynamical matrix for the full system, there are contributions to $F_1(\omega)$ over a wide range of frequencies. Despite this, there is a strong response at the driving frequency ω_0. We also show the Fourier transform $F_3(\omega)$ of the x displacement of the input disk 3 and calculate the gain $G(\omega_0) = F_1(\omega_0)/F_3(\omega_0)$. We find that the gain in this high-pressure regime is independent of the amplitude of the driving [see Fig. 8(b)]. The gain for the on state at high pressure $p = 10^{-1}$ is $G(\omega_0) \approx 1$, whereas the gain for the off state at lower pressure $p = 3.2 \times 10^{-2}$ is more than two orders of magnitude smaller. In Fig. 9(a), we show the variation of the gain $G(\omega_0)$ with pressure for several values of the driving frequency ω_0. We verify that we can accurately measure the gain ($G(\omega_0) \approx 3.5$) near each resonance in Fig. 9(b). For each driving frequency, $\omega_0 = 13.1$, 14.9, and 15.7, the ratio of the maximum gain (at p_{on}, on state) and minimum gain (at p_{off},
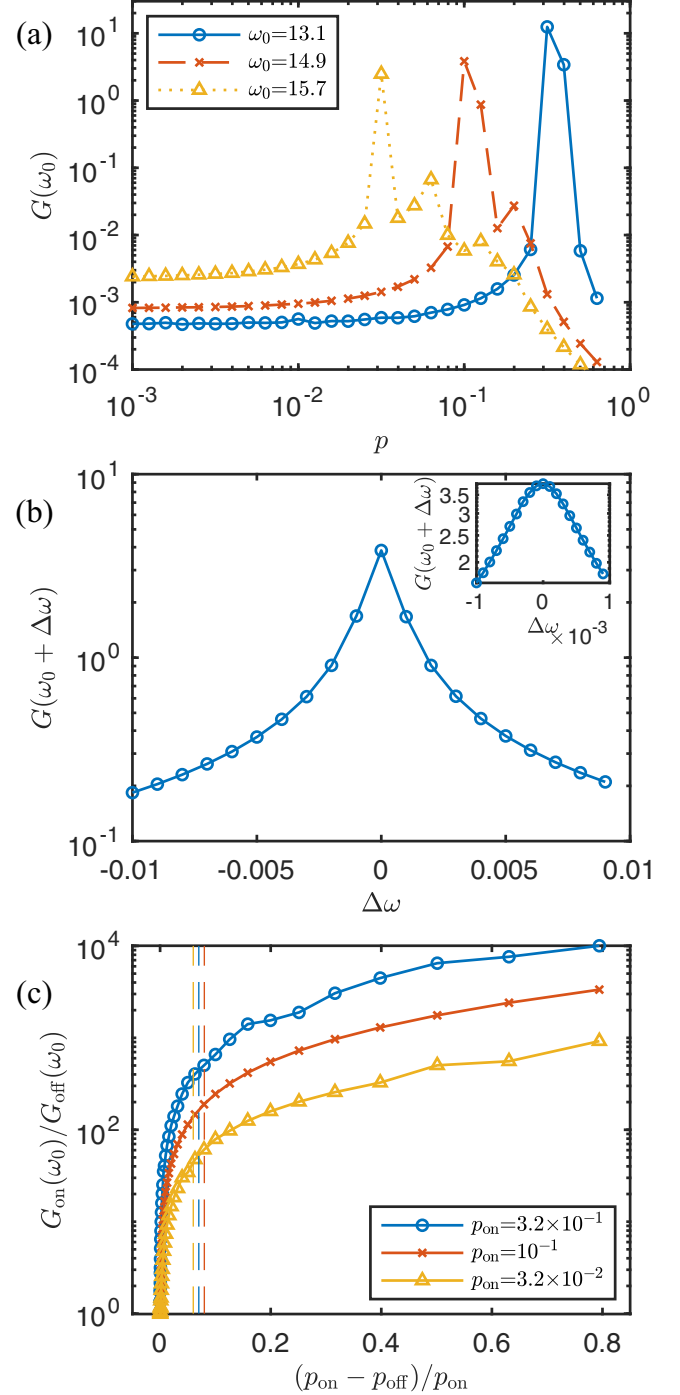

FIG. 9. (a) The gain $G(\omega_0)$ for the acoustic device as a function of pressure p for three values of the driving frequency $\omega_0 = 13.1$ (circles), 14.9 (Xs), and 15.7 (triangles). (b) The gain $G(\omega_0 + \Delta\omega)$ over a small frequency range $\Delta\omega$ near the driving frequency $\omega_0 = 14.9$. The inset is a close-up of the gain to within 10^{-3} of ω_0. (c) The gain ratio $G_{\text{on}}(\omega_0)/G_{\text{off}}(\omega_0)$ as a function of the normalized change in pressure between the on and off states, $(p_{\text{on}} - p_{\text{off}})/p_{\text{on}}$, for $p_{\text{on}} = 3.2 \times 10^{-1}$ (circles), 10^{-1} (Xs), and 3.2×10^{-2} (triangles) and the sizes of all particles are changed to control the pressure. The vertical dashed lines indicate the value of $(p_{\text{on}} - p_{\text{off}})/p_{\text{on}}$ at which contacts would begin breaking if the size of only a single particle was changed to control the pressure. For all data, the driving amplitude is $A_0 = 10^{-6}$ and the damping parameter $b = 10^{-3}$.
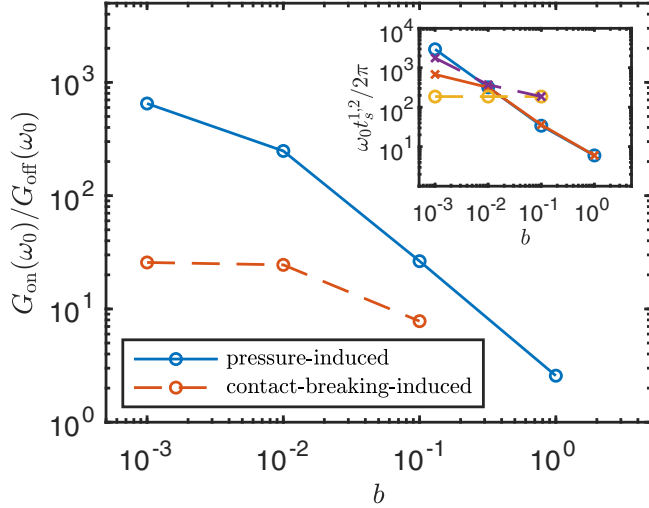
FIG. 10. The gain ratio $G_{on}(\omega_0)/G_{off}(\omega_0)$ between the on and off states versus the damping parameter b at fixed driving frequency $\omega_0 = 14.9$ for pressure-induced switching (solid line) and 16.0 for switching with contact breaking (dashed line). The inset shows the switching time $\omega_0 t_s^1/2\pi$ from the on to the off state (open circles) and $\omega_0 t_s^2/2\pi$ from the off to the on state (Xs) versus b for the same systems in the main panel.

off state) increases as a function of the normalized pressure difference $(p_{on} - p_{off})/p_{on}$. For $\omega_0 = 15.9$, the increase in the gain ratio $G_{on}(\omega_0)/G_{off}(\omega_0)$ is the largest, reaching 10^4 at the largest pressure difference [see Fig. 9(c)]. We can also vary the gain ratio between the on and off states at fixed driving frequency ω_0 by changing the damping coefficient b. In Fig. 10, we show that the gain ratio decreases as a power law with the damping parameter, $G_{on}(\omega_0)/G_{off}(\omega_0) \sim b^{-1}$ for large b. In contrast, the gain ratio plateaus in the limit of small b.

We have demonstrated that we can achieve gain ratios between the on and off states for the acoustic device that are at least four orders of magnitude. We will now analyze the ability of the device to switch from the on to off states and vice versa. We will change the sizes of all particles in the device to instantaneously increase or decrease the pressure and induce switching. In Fig. 11(a), we show the Fourier transform $F_1(\omega_0)$ of the x displacement of disk 1, while driving disk 3 sinusoidally at ω_0 in the x direction. We consider two situations: (1) The device is initiated in the on state at pressure $p = 10^{-1}$. The system remains in the on state for a given amount of time. At time t^*, the system is switched to the off state by decreasing the pressure to 3.2×10^{-2} and remains there. (2) The device is initiated in the off state at $p = 3.2 \times 10^{-2}$ and remains in the off state for a given amount of time. At time t^*, the pressure is increased to $p = 10^{-1}$ and remains there. In Fig. 11(a), we show that for the case of pressure-induced switching, the switching time t_s from on to off and from off to on are comparable. For damping parameter $b = 10^{-2}$, $\omega_0 t_s/2\pi \approx 10^3$, where t_s is obtained by determining the time at which $F_1(\omega_0)$ reaches the geometric mean of the values of $F_1(\omega_0)$ in the on and off states.

Note that the switching time t_s is rather large ($\sim 10^3$ oscillations for $b = 10^{-2}$). This large timescale occurs because the oscillation of a single input particle and a single output
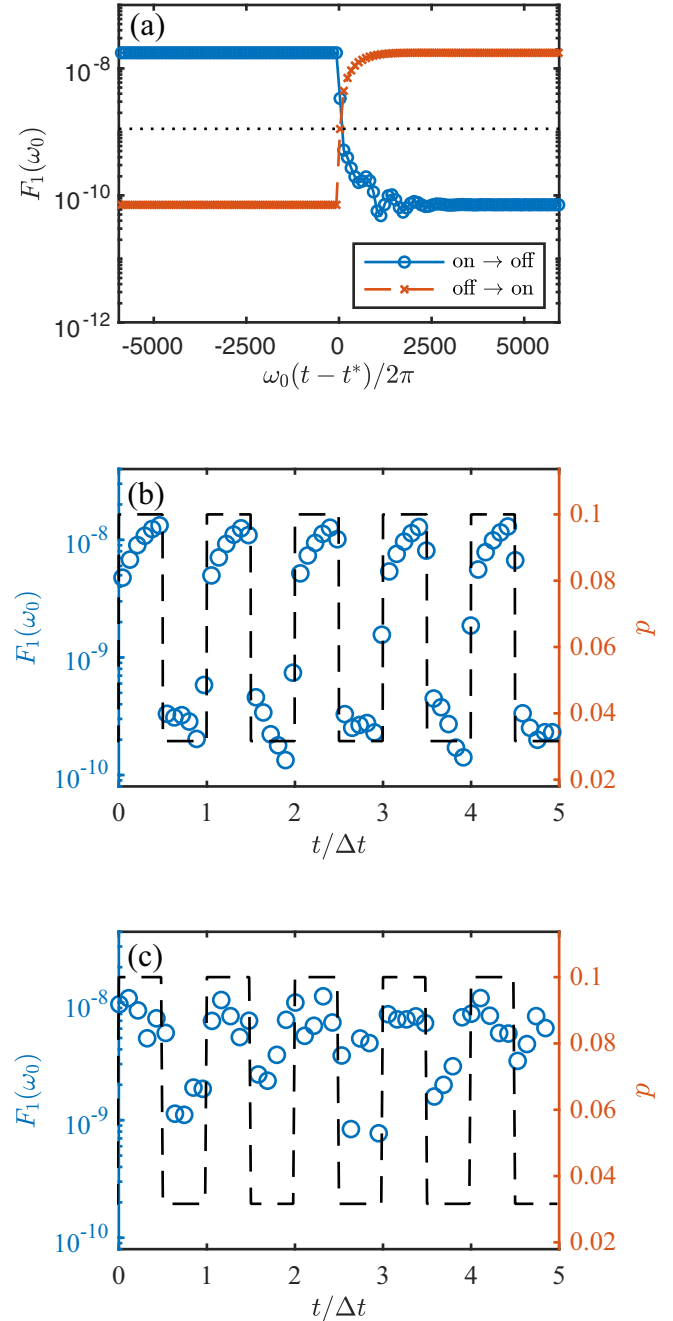

FIG. 11. (a) The Fourier transform $F_1(\omega_0)$ of the x displacement of disk 1 as a function of time $\omega_0(t - t^*)/2\pi$ when switching the device at time t^* from the "on" (pressure $p = 10^{-1}$) to "off" ($p = 3.2 \times 10^{-2}$) states (circles) and vice versa (Xs) using a damping coefficient $b = 10^{-2}$. The horizontal dotted line indicates the geometric mean $\overline{F}_1(\omega_0)$ of the on and off values of $F_1(\omega_0)$. The switching times t_s are obtained by finding when $F_1(\omega_0)$ crosses $\overline{F}_1(\omega_0)$. (b) The Fourier transform $F_1(\omega_0)$ (open circles and left axes labels) of the x displacement of disk 1 as a function of time $t/\Delta t$ (after reaching an initial steady state at $t = 0$) during continuous switching of the device between the "on" and "off" states using $b = 10^{-2}$. The pressure of the device (dashed line and right axes labels) follows a square-wave signal with $\Delta t/t_s \approx 3.7$. (c) Same as (b) except $\Delta t/t_s \approx 0.7$.

particle are not pure eigenmodes of the mass-weighted dynamical matrix of the device. Thus, when switching from the on to off state, there is residual energy in the eigenmode at ω_0 that must be removed via damping. When switching from the off to on state, there is residual energy in eigenmodes that are different from the one at ω_0 that must be removed via damping. This picture is consistent with the fact that the switching timescale as $\omega_0 t_s \sim b^{-1}$ as shown in the inset to Fig. 10 (solid lines). With this scaling behavior, t_s can be decreased by increasing b. However, as shown in Fig. 10, the gain ratio also decreases with increasing b, which makes it difficult to distinguish between the on and off states. Thus, the optimal performance for the pressure-induced acoustic switch is the relatively small value for the damping parameter, $b \approx 10^{-2}$, where the gain ratio no longer increases dramatically with decreasing b, yet t_s is relatively small.

We also studied dynamic switching using a square-wave input signal for the time dependence of the pressure. In this case, the pressure is large for given amount of time Δt and then it is switched instantaneously to a lower pressure for a time period Δt. After an additional time period Δt, the pressure is again switched back to the large pressure value. This process is then repeated for a given number of cycles. [See the dashed lines in Figs. 11(b) and 11(c).] When Δt satisfies $\Delta t \gtrsim t_s$, $F_1(\omega_0)$ tracks with the pressure signal and is nearly able to reach the steady-state values of $F_1(\omega_0)$ at each pressure as shown in Fig. 11(b). [The steady-state values of $F_1(\omega_0)$ are $\approx 2 \times 10^{-8}$ for the on state and $\approx 8 \times 10^{-11}$ for the off state.] For $\Delta t \lesssim t_s$, $F_1(\omega_0)$ is not able to track the input signal [as shown in Fig. 11(c)] and thus the gain ratio between the on and off states for dynamic switching is much smaller than the gain ratio in steady state. The case $\Delta t \gg t_s$ is similar to the step function perturbation in Fig. 11(a).

B. Switching with contact breaking

In this subsection, we describe the results for acoustic devices where switching between the on and off states is achieved by changing the network of interparticle contacts. In the systems we consider, the interparticle contact network does not change during the vibrations in the on state. However, the interparticle contact network fluctuates during the vibrations in the off state. In Fig. 12(a), we show the Fourier transform $F_1(\omega)$ of the x displacement of disk 1 for the device in the low-pressure regime with $p = 10^{-6}$ (on state) and 10^{-8} (off state) obtained by driving disk 3 sinusoidally with amplitude $A_0 = 3.2 \times 10^{-7}$ and frequency $\omega_0 = 16.0$, using damping coefficient $b = 10^{-3}$. $F_1(\omega)$ for the device at $p = 10^{-6}$ is similar to that in the high-pressure regime [Fig. 8(a)]. However, $F_1(\omega)$ at $p = 10^{-8}$ has a broad and noisy spectrum since the interparticle contact network fluctuates during the vibrations. [See the contact-breaking regime for $D(\omega)$ in Fig. 5(b).] In the low-pressure regime, the device can be switched on and off by varying the amplitude of the driving at fixed frequency ω_0. In Fig. 12(b), we show the gain $G(\omega_0)$ of the device at pressures $p = 10^{-6}$ and 10^{-8} and driving frequency $\omega_0 = 16.0$. At small driving amplitudes, the gain is relatively large, $G(\omega_0) \approx 1$. As the amplitude is increased, changes in the interparticle contact network begin to occur at a characteristic amplitude A_0^* that scales with pressure.
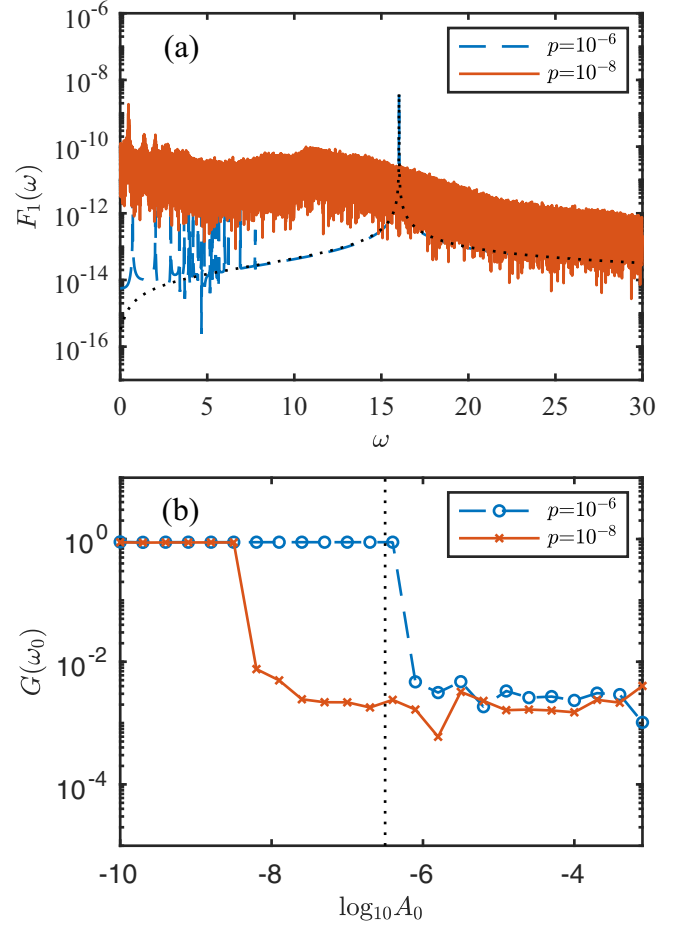

FIG. 12. (a) The Fourier transform $F_1(\omega)$ of the x displacement of disk 1 for the device with pressure $p = 10^{-6}$ (dashed line) and 10^{-8} (solid line) obtained by driving disk 3 sinusoidally with amplitude $A_0 = 3.2 \times 10^{-7}$ and frequency $\omega_0 = 16.0$, using damping coefficient $b = 10^{-3}$. The dotted line shows the Fourier transform $F_3(\omega)$ of the x displacement of the input disk 3. (b) The gain $G(\omega_0)$ [defined in Eq. (4)] plotted as a function of the driving amplitude A_0 with driving frequency $\omega_0 = 16.0$ for a device at pressure $p = 10^{-6}$ (dashed line) and 10^{-8} (solid line), using damping parameter $b = 10^{-3}$. The vertical dotted line indicates the amplitude of the driving $A_0 = 3.2 \times 10^{-7}$ in (a).

See Fig. 6(b) for a device in which the interparticle contact network has fewer contacts in the off state than in the on state. For example, $A_0^* \approx 10^{-8.5}$ for $p = 10^{-8}$ and $A_0^* \approx 10^{-6.5}$ for $p = 10^{-6}$. The onset of contact breaking causes the gain to drop abruptly by more than two orders of magnitude. We show in Fig. 12(b) that if we drive the device at amplitude $A_0 = 3.2 \times 10^{-7}$ and frequency ω_0, it is in the on state at pressure $p = 10^{-6}$ and the off state at 10^{-8}. We can obtain similar behavior if we drive the device in the amplitude range $5 \times 10^{-9} \lesssim A_0 < 3.2 \times 10^{-7}$.

We show the ratio of the gain in the on versus the off state $G_{on}(\omega_0)/G_{off}(\omega_0)$ as a function of the damping parameter b for devices that experience contact breaking in Fig. 10. As for devices with no contact breaking, the gain ratio decreases with b for large b, whereas it forms a plateau for small b. However, at small b, the gain ratio is nearly two orders

of magnitude smaller for devices that incorporate contact breaking compared to those that do not.

In Fig. 13(a), we show the performance of the acoustic device in switching from the on to off states and vice versa using damping parameter $b = 10^{-3}$ in the regime where contact breaking occurs. An interesting feature is that the times t_s^1 and t_s^2 for switching the device from the on to the off state and from the off to the on state, respectively, are different. As shown in the inset in Fig. 10, the switching time from the on to the off state, $\omega_0 t_s^1 / 2\pi \sim 10^2$, is nearly independent of the damping parameter b, and is less than the switching time from the off to the on state ($t_s^1 < t_s^2$) since t_s^2 grows with decreasing b.

We show the results for dynamic switching with contact breaking for the device in Fig. 13(b) for the case $\Delta t / t_s^1 \approx 2.7$. $F_1(\omega_0)$ can roughly track the pressure signal, but the signal for the off state is noisy. When we decrease Δt such that $\Delta t / t_s^1 \approx 0.68$, there is no significant difference between $F_1(\omega_0)$ in the on and off states and $F_1(\omega_0)$ is not strongly affected by the relatively rapid changes in pressure.

C. Single-particle control signal

For systems without contact breaking, the gain ratio between the on and off states $G_{\mathrm{on}}(\omega_0)/G_{\mathrm{off}}(\omega_0)$ is determined by the difference in pressure that can be achieved, for example, by changing all particle sizes. In Fig. 9(c), we showed that the gain ratio increases with the normalized pressure difference $(p_{\mathrm{on}} - p_{\mathrm{off}})/p_{\mathrm{on}}$. When we use all particles in the device to change the pressure, we can achieve a wide range of normalized pressure differences from 0 to 0.8, and thus we can obtain a wide range of gain ratios from 1 to 10^4. However, when we use only a single control particle [e.g., the central grain in Fig. 6(b)], the maximum change in the normalized pressure that can be achieved scales as $1/N$. In Fig. 14, we show that for $N = 30$, the maximum normalized pressure difference is $\sim 10^{-1}$ using a single control particle. Operating the device in the regime where the interparticle contact network remains intact further restricts the normalized pressure difference that can be used. If we limit $(p_{\mathrm{on}} - p_{\mathrm{off}})/p_{\mathrm{on}} < 10^{-1}$, the maximum gain ratio that can be achieved is $G_{\mathrm{on}}(\omega_0)/G_{\mathrm{off}}(\omega_0) \approx 10^{2.5}$, which is less than the value of 10^4 achieved for devices that change the sizes of all particles. [See the vertical lines in Fig. 9(c).]

As expected, the performance of devices that only have a single control particle is also degraded in the regime where contact breaking occurs. In Fig. 15(a), we show the gain $G(\omega_0)$ for a device driven at frequency $\omega_0 = 16.0$ versus the amplitude A_0 and compare it to the gain from systems in which the size of a single control particle has been decreased by an amount $\Delta\sigma/\sigma$. The reference system (with $\Delta\sigma/\sigma = 0$) is in the on state with $G(\omega_0) \approx 1$ for small driving amplitudes. As the driving amplitude increases, the gain decreases abruptly when the interparticle contact network begins to fluctuate. Similar behavior is found in Fig. 12(b). When the change in the size of the control particle is small, i.e., $\Delta\sigma/\sigma = 5.1 \times 10^{-7}$, $G(\omega_0)$ is similar to that for the reference system. When $\Delta\sigma/\sigma$ is increased further, $G(\omega_0)$ develops an intermediate plateau between that for the on state [$G(\omega_0) \approx 1$] and the off state [$G(\omega_0) \approx 10^{-3}$]. Thus, by changing the size of only one
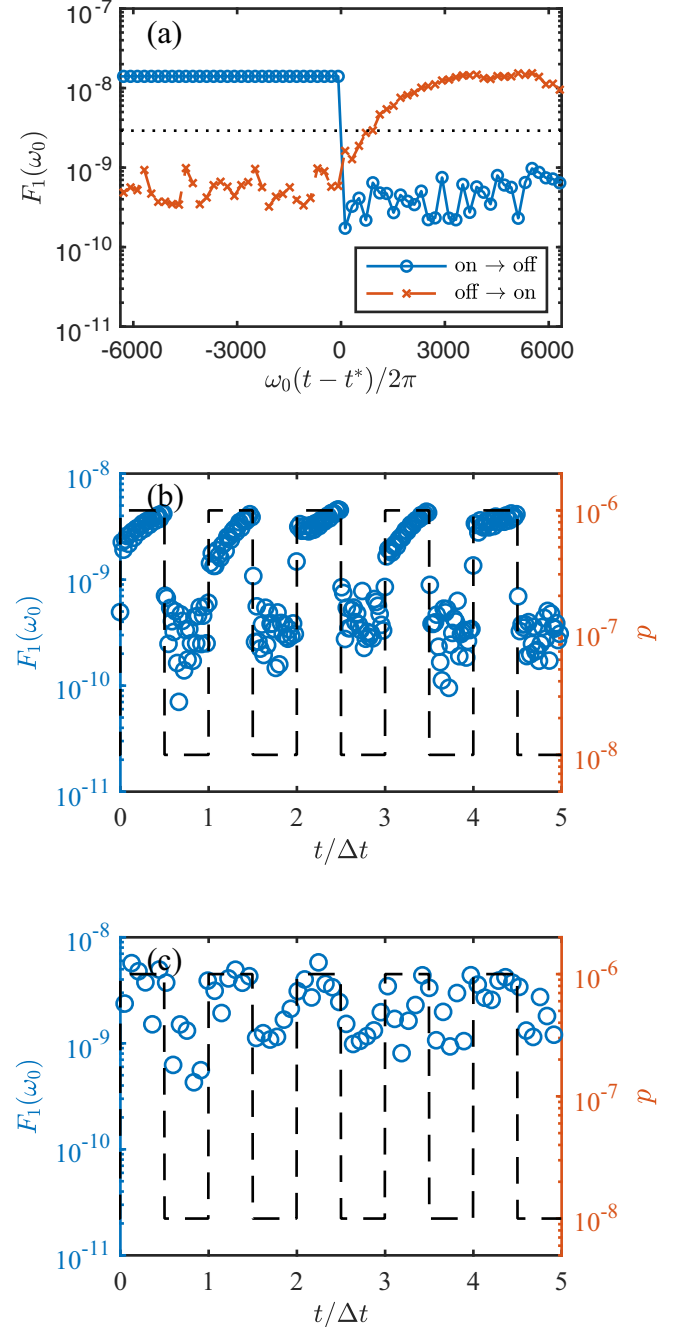

FIG. 13. (a) The Fourier transform $F_1(\omega_0)$ of the x displacement of disk 1 as a function of time $\omega_0(t - t^*)/2\pi$ when switching the device from the "on" (pressure $p = 10^{-6}$) to "off" ($p = 10^{-8}$) states (circles) and vice versa (Xs) at time t^* using a damping coefficient $b = 10^{-3}$. The driving frequency and amplitude are $\omega_0 = 16.0$ and $A_0 = 3.2 \times 10^{-7}$. (b) The Fourier transform $F_1(\omega_0)$ of the x displacement of disk 1 (circles and left axes labels) as a function of time $t/\Delta t$ when continuously switching the device between the "on" and "off" states using $b = 10^{-3}$. The dashed line shows the pressure of the device (right axes labels), which has a square-wave form with $\Delta t / t_s \approx 2.7$ (where t_s is the time for the device to switch from the off to the on states). (c) Same as (b) except $\Delta t / t_s \approx 0.68$. For (a)–(c), the off and on states possess different interparticle contact networks.
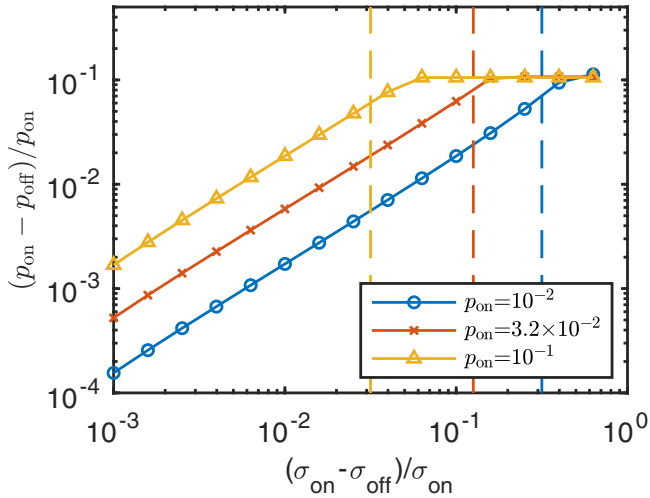
FIG. 14. The normalized change of pressure $(p_{on} - p_{off})/p_{on}$, where p_{on} and p_{off} are the pressures in the on and off states, respectively, as a function of the normalized change in the size $(\sigma_{on} - \sigma_{off})/\sigma_{on}$ of a single control particle for pressures $p_{on} = 10^{-2}$ (circles), 3.2×10^{-2} (Xs), and 10^{-1} (triangles). The vertical dashed lines (from left to right) indicate the change in size above which the control particle loses a contact with neighboring particles for $p_{on} = 10^{-2}$, 3.2×10^{-2}, and 10^{-1}.

particle, a dynamic state with an intermediate value of the gain occurs. This intermediate state represents a system in which only the contacts that involve the control particle (not all interparticle contacts) are fluctuating. As shown in Fig. 15(b), the presence of the state with intermediate gain significantly reduces the difference in $F_1(\omega_0)$ between the on and off states during switching. For all changes in pressure that can be achieved using a single control particle and induce contact breaking between the control particle and its neighbors, we find a dynamical state with intermediate gain between that for the on state (with no contact breaking) and off state (with contact breaking among all particles).

D. Generating 2D granular crystals

In Sec. III A, we described the performance of acoustic switching devices composed of $N = 30$ monodisperse disks (with diameter σ) of two different masses ($N_L = 21$ with mass m_L and $N_S = 9$ with mass m_S) arranged on a two-dimensional hexagonal lattice similar to that in the inset of Fig. 4. To realize these devices in experiments, an automated method of making the 2D granular crystals must be developed. Methods for generating granular crystals in experiments include vibration [22], cyclic shear [23], and combinations of vibration and shear [24]. However, it is well known that generating defect-free granular crystals is difficult, requiring an exponentially large number of small amplitude vertical vibrations or shear cycles [25]. Further, one way to generate a large frequency band gap in granular crystals is to choose grains with large mass ratios. However, vibration and shear in systems composed of grains with large mass ratios often give rise to demixing or segregation, where grains with similar masses cluster together [26,27], instead of forming the alternating pattern of grains with large and small masses shown in the
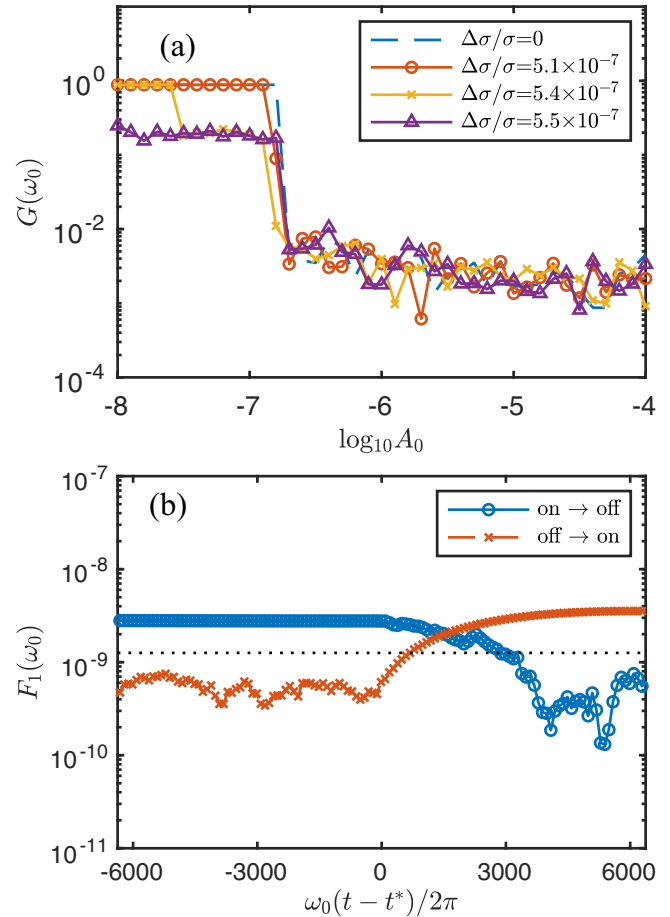

FIG. 15. (a) The gain $G(\omega_0)$ [defined in Eq. (4)] plotted as a function of the driving amplitude A_0 at fixed driving frequency $\omega_0 = 16.0$ for a device with a single control particle at $\Delta\sigma/\sigma = 0$ (dashed line), 5.1×10^{-7} (circles), 5.4×10^{-7} (Xs), and 5.5×10^{-7} (triangles), using damping parameter $b = 10^{-3}$. (b) The Fourier transform $F_1(\omega_0)$ of the x displacement of disk 1 as a function of time $\omega_0(t - t^*)/2\pi$ when switching the device from the on ($\Delta\sigma/\sigma = 0$) to off ($\Delta\sigma/\sigma = 5.4 \times 10^{-7}$) state (circles) and vice versa (Xs) at time t^* using a single control particle and damping parameter $b = 10^{-3}$. The driving frequency and amplitude are $\omega_0 = 16.0$ and $A_0 = 6.3 \times 10^{-8}$, respectively.

inset of Fig. 4 that maximizes the width of the frequency band gap.

In this subsection, we describe a method to enhance crystallization into the alternating pattern of grains shown in the inset to Fig. 4, implement it in numerical simulations, and provide an estimate for how long it would take to generate the alternating disk pattern in experiments. We consider mixtures of $N_L = 21$ disks with diameter σ and $N_S = 9$ disks with the same size and mass of the others, but they possess small circular knobs symmetrically placed around their perimeter (see Fig. 16). The knobs have diameter $\sigma_k = (2\sqrt{3}/3 - 1)\sigma$ and the angular separation between the knobs is $2\pi/n$, where $n = 0$, 3, and 6 gives the number of knobs. The size and spacing of the knobs is chosen so that they fit within the interstices of the circular grains without knobs arranged on a hexagonal lattice. The knobs will only fit within the interstices when they are surrounded by grains without knobs
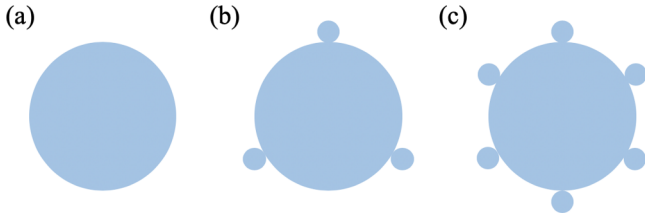
FIG. 16. Circular particles with different numbers of circular knobs, (a) $n = 0$, (b) 3, and 6, placed symmetrically around the perimeter of the particle. The central disk has diameter σ and the circular knobs have diameter $\sigma_k = (2\sqrt{3}/3 - 1)\sigma$.

(see Fig. 17). Thus, in mixtures of grains with and without knobs, there is an effective repulsion between grains with knobs that enhances crystallization into the alternating pattern in the inset of Fig. 4.

As we will show below, we are able to create packings in which grains with knobs and grains without knobs form an alternating pattern on a hexagonal lattice. If, in experiments, the grains with knobs are made of a composite material for which part of the material can be preferentially dissolved, then the knobs, as well as part of the core of the grain, can be dissolved after the hexagonal assembly has been generated. Thus, this procedure can generate an alternating pattern of light and heavy grains.

To measure the degree to which a disk configuration in the simulations matches the alternating pattern in the inset to Fig. 4, we determine the number of contacting pairs of grains with knobs, N_{kk}, of the inherent structures. To calculate the inherent structures, we take instantaneous snapshots from the discrete element method simulations and perform steepest descent (with the knobs removed) to reach the nearest local potential energy minimum for each snapshot. The alternating pattern in the inset to Fig. 4 has $N_{kk} = 0$, and $N_{kk} > 0$ for configurations in which the particle positions differ from those for the alternating pattern. In Fig. 17, we show an instantaneous snapshot from the discrete element method simulations [Fig. 17(a)] and its associated inherent structure with $N_{kk} = 0$ [Fig. 17(b)]. Figure 17(c) shows a more disordered inherent structure with $N_{kk} = 7$.

Note that there are some configurations with $N_{kk} = 0$ that do not perfectly match the alternating pattern in the inset
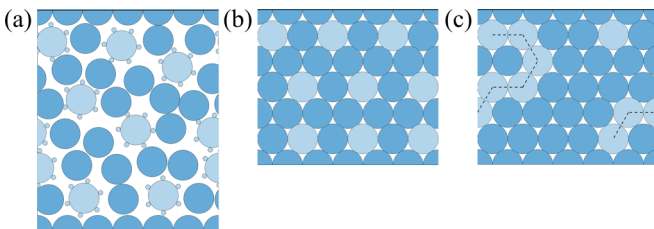

FIG. 17. (a) Snapshot of a disk configuration generated using the accelerated discrete element method simulations after four rounds of acceleration. The light disks have $n = 6$ knobs and the dark disks have zero knobs. The inherent structures with zero kinetic energy and (b) $N_{kk} = 0$ and (c) 7 were obtained after removing the knobs. Contacts between the light-colored grains in (c) are indicated by the dotted lines.
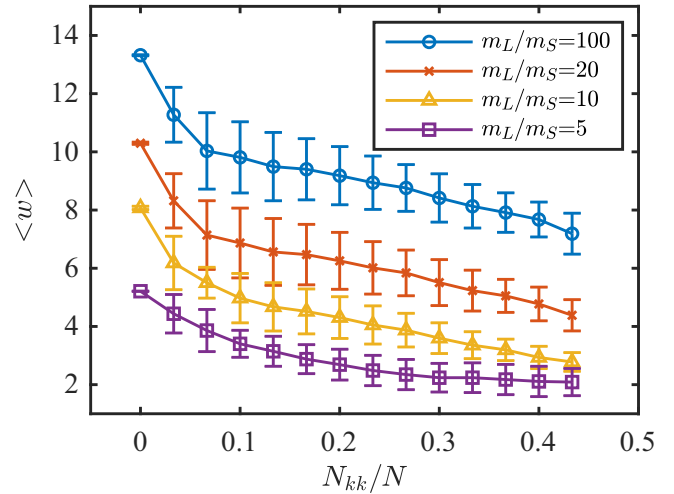

FIG. 18. The average maximum difference between adjacent eigenfrequencies $\langle w \rangle$ of the mass-weighted dynamical matrix versus the number of contacts between the grains with knobs N_{kk}/N for a hexagonal packing with $N_L = 21$ and $N_S = 9$ and mass ratio $m_L/m_S = 100$ (circles), 20 (Xs), 10 (triangles), and 5 (squares). The means and standard deviations (error bars) are obtained by averaging over 50 configurations in which the masses of the grains are chosen randomly as either m_L and m_S to yield a given N_{kk}/N.

to Fig. 4 [e.g., the configuration in Fig. 17(b)]. However, we show in Fig. 18 that the average width of the bandgap $\langle w \rangle$ is well defined when we average over an ensemble of configurations with the same N_{kk}.

As previously shown in Fig. 4, w increases with the mass ratio m_L/m_S. In addition, we find that $\langle w \rangle$ increases as $N_{kk} \to 0$, reaching a maximum that depends on the mass ratio. Thus, especially for small mass ratios, it is necessary to have packings with $N_{kk} \to 0$ to achieve robust band gaps. In Appendix B, we discuss the performance of acoustic switching devices (made from 2D granular crystals) with small band gaps.

To generate static packings of grains with and without knobs, we first performed discrete element method simulations at constant pressure beginning at high temperature in the liquid state and then cooled the system to low temperature as a function of the cooling rate, which we adjusted by varying the damping parameter b. The interactions between the large circular disks, between the large disks and small knobs, and between the small knobs have the same form as Eq. (1). Even though we varied the cooling rate over more than four orders of magnitude, we did not find a significant decrease in N_{kk}/N from its value in the liquid state ($N_{kk} > 6$) for $n = 0$, 3, and 6.

To obtain configurations with small N_{kk}/N, we implemented an umbrella sampling method to enhance the probability of rare events [28–30]. We started with 10 independent liquidlike configurations with $N_{kk}/N \approx 0.21$ for their inherent structures. For each of the 10 configurations, we generated 10 systems with the same particle positions, but different random velocities. For each of these systems, we performd constant pressure simulations at a sufficiently high temperature to explore different configurations over $N_{sim} = 10^6$ time steps. During the simulation, we record the 10 snapshots with the
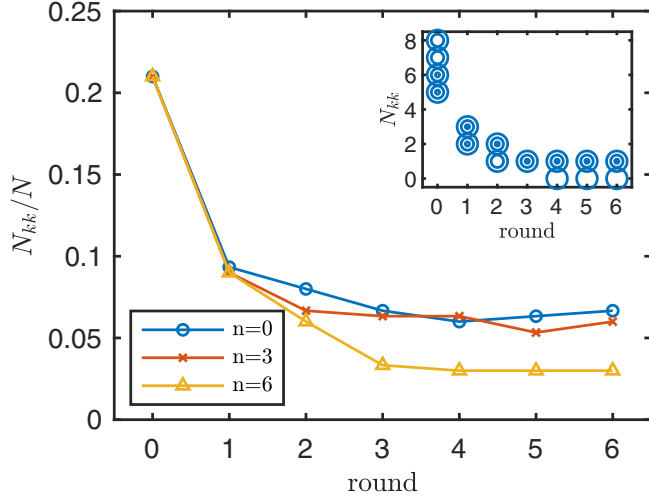
FIG. 19. The average N_{kk}/N from inherent structures as a function of the number of rounds of the accelerated MD simulations for the systems in Fig. 17 with $n = 0$ (circles), 3 (Xs), and 6 (triangles) knobs. The inset shows a scatter plot of N_{kk} versus the number of rounds for the system with $n = 6$ knobs.

smallest N_{kk} for their inherent structures. This constitutes round 1. For each snapshot, we rescale the temperature by a factor of 0.95 and use these as initial conditions in constant pressure simulations and run the simulations at the new temperature for N_{sim} time steps. Successive rounds of selecting configurations with the smallest N_{kk} and running them at lower temperatures are carried out until N_{kk} does not further decrease. We show N_{kk}/N versus the number of acceleration rounds in Fig. 19 for mixtures of grains with $n = 0$, 3, and 6 knobs. We find that having six knobs allows the system to reach smaller values of N_{kk} than mixtures of grains with $n = 0$ and 3 knobs.

As shown in Fig. 17, the umbrella sampling method can achieve configurations with $N_{kk} = 0$ for the inherent structures after four acceleration rounds for mixtures with $n = 6$ knobs. We will now estimate the time required to achieve inherent structures with $N_{kk} = 0$ in typical experiments of vibrated granular media. In the discrete element method simulations, we used a time step of $\Delta t_s = 1.6 \times 10^{-4}$ s, using the characteristic timescale $\tau_s = \sqrt{m\sigma/\epsilon} = 0.032$ s. For millimeter-sized steel beads frequently used in experiments on granular media, the characteristic timescale is $\tau_e = \sqrt{M/K_e} \approx 2.1$ μs, where $M = 10$ g is the mass, $K_e = ER_0/(1 - \nu^2)$ is the stiffness, $R_0 \approx 10$ mm is the raidus, $E \approx 200$ GPa is the Young's modulus, and $\nu \approx 0.3$ is the Poisson's ratio. Using these values, the simulation time step corresponds to a time step of $\Delta t_e = (\tau_e/\tau_s)\Delta t_s \approx 0.01\mu$s for experiments on vibrated mm-sized steel beads.

After four rounds of acceleration, the probability to achieve an inherent structure with $N_{kk} = 0$ is $P = 10^{-8}$. Since snapshots from the simulations were recorded every 10^5 time steps out of a total of 10^6, the elapsed time between configurations with $N_{kk} = 0$ is between $10^5\Delta t_e \approx 1$ ms and $10^6\Delta t_e \approx 10$ ms. Thus, the average time required to achieve a configuration with $N_{kk} = 0$ in vibration experiments is between 1 ms$/10^{-8} \approx 1$ day and 10 ms$/10^{-8} \approx 10$ days. These time

periods are achievable in expermiental studies of granular media, and can be further reduced by carrying out vibration studies on multiple experimental set-ups in parallel.

IV. CONCLUSIONS AND FUTURE DIRECTIONS

In this article, we describe active acoustic transistor-like devices that can switch from the on to off states or vice versa using 2D granular crystals. We focus on systems composed of two types of grains with the same size but different masses, since they possess frequency band gaps in the vibrational density states that can be tuned by the mass ratio m_L/m_S and arrangement of heavy and light grains. The input signal is generated by oscillating a grain at one side of the device and measuring the resulting output signal from a grain on the other side of the device. The device can be switched between the on and off states by changes in the size of one or many grains, which controls the pressure. Switching can be achieved through two mechanisms: (1) pressure-induced switching in which the on and off states have the same interparticle contact networks and (2) switching with contact breaking, where the interparticle contact networks are different in the on and off states. In general, we find that the performance of pressure-induced switching is better, with larger gain ratios between the on and off states, than those for switching with contact breaking. However, there is a trade-off between large gain ratios and fast switching times. Large gain ratios occur at small damping parameters and fast switching times occur at larger damping parameters. Even so, for pressure-induced switching, 2D granular crystals can achieve gain ratios greater than 10^4, and switching times $\omega_0 t_s$ that represent 10^3 oscillations at the driving frequency. This switching time is comparable to that obtained recently for sonic crystals [1] and less than that for photonic transistor devices [31].

Granular crystals are difficult to make in an automated way in experiments. We thus developed techniques to improve the efficiency of making hexagonal crystals with an alternating pattern of heavy and light grains. The first improvement involved studying mixtures of grains with and without small knobs arranged on their perimeter. The size and arrangement of the knobs are chosen so that they fit in the intertices between contacting grains without knobs. Since the grains with knobs do not pack efficiently when they are next to each other, there is an effective repulsion between the grains with knobs. The similarity between a given configuration and the optimal configuration with an alternating pattern can be measured using the fraction of contacts between grains with knobs, N_{kk}/N.

Using conventional discrete element method simulations of these mixtures undergoing cooling at fixed pressure, N_{kk} does not decrease significantly with temperature. However, when we apply an umbrella samplinglike technique, we find that we can achieve $N_{kk}/N \to 0$. Further, we show that grains with $n = 6$ knobs leads to smaller values of N_{kk} than that with $n = 3$ when cooling with umbrella sampling. Based on the probability for obtaining configurations with $N_{kk} = 0$ in the accelerated simulations, we estimate that it will take from 1 to 10 days to achieve an $N_{kk} = 0$ packing of millimeter-sized sized steel beads using vibration experiments. This time

period can be further reduced by running a number of vibration experiments in parallel.

Thus, these results will encourage experimental studies of mixtures of grains with and without knobs undergoing vibration or cyclic shear to study crystallization into hexagonal crystals. After generating the alternating pattern of grains with and without knobs, the core regions of the grains with knobs and the knobs themselves can be dissolved away, yielding $m_L/m_S > 1$. Experiments can then be performed to measure the vibrational density of states in these crystalline granular assemblies.

There are a number of important directions that we will pursue in future studies. First, we will consider 3D granular crystals, which have a broader range of mechanically stable crystal structures with different symmetries, packing fractions, and numbers of nearest neighbors. For example, we will determine the performance of FCC, BCC, and HCP crystals with different mass distributions. Second, in the current study, both the input and output signals oscillated in the x direction. In future studies in 3D, we can consider an input signal that oscillates in a different direction than the measured output signal. A key aspect of these studies will be to understand the spatial structure of the eigenmodes of the mass-weighted Hessian of the device, and their overlap with the input and output signals. Third, in the current modeling studies, we neglected static friction. However, granular crystals in experiments have finite friction, and thus it is important to understand how static friction and the coupling of particle rotation and translation affect the switching performance of the device. Fourth, an interesting application is to create logical circuits from coupled acoustic switches that connect the output of one device to the input of another. In future studies, we will develop numerical implementations of coupled 2D granular crystals that can perform logical operations.

APPENDIX A: ROBUSTNESS OF THE MEASUREMENT OF THE FOURIER TRANSFORMS OF THE INPUT AND OUTPUT SIGNALS

Many of the results reported in this article depend on the accurate calculation of the Fourier transform of the input and output signals from particles 1 and 3, $x_{1,3}(t) - x_{1,3}^0$, respectively, where $x_{1,3}^0$ is the x position of particles 1 and 3 in the initial mechanically stable packing. We calculate the Fourier $F_{1,3}(\omega) = \int_0^\infty [x_{1,3}(t) - x_{1,3}^0]e^{i\omega t}dt$ numerically via the discrete Fourier transform:

$$F_{1,3}[\omega(l)] = \sum_{n=0}^{M-1}[x_{1,3}(n\Delta) - x_{1,3}(0)]e^{-i\cdot 2\pi ln/M}, \quad (A1)$$

where $\omega(l) = 2\pi l/T$, $M = T/\Delta$, l, and n are integers, T is the total time of the input-output signals, and Δ is the time interval between samples. In this Appendix, we calculate the gain $G(\omega_0)$ as a function of the total time T and sampling time Δ of the input and output signals to show that our calculations do not depend strongly on these parameters.
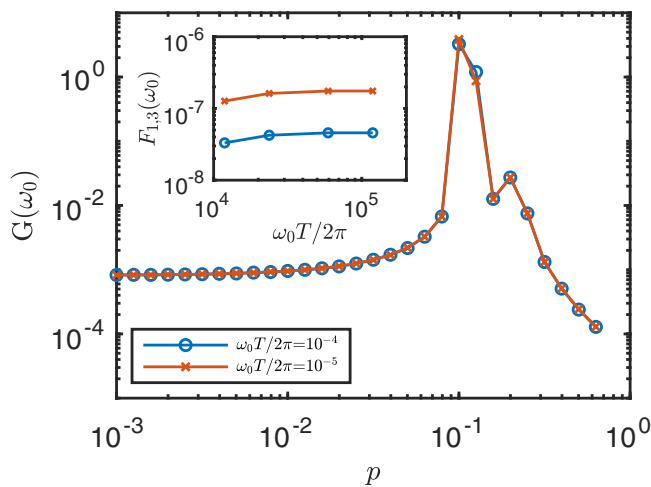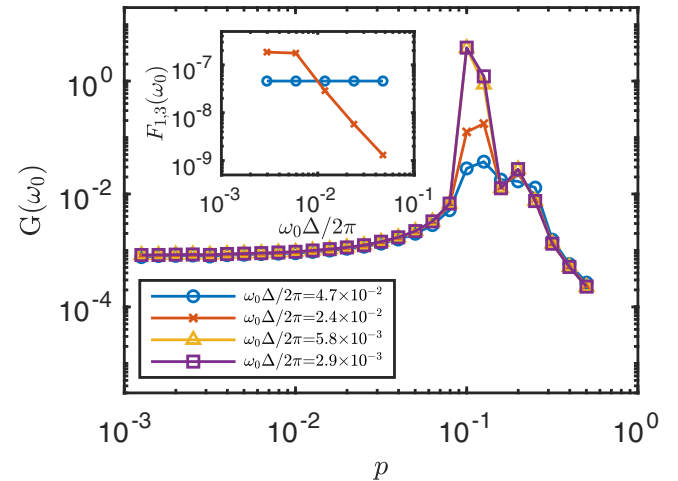

FIG. 20. The gain $G(\omega_0)$ for the acoustic device as a function of pressure p (for a system with no contact breaking) using a total simulation time $\omega_0 T/2\pi = 10^4$ (circles) and 10^5 (squares). The inset shows the Fourier transforms of the output and input signals, $F_1(\omega_0)$ (Xs) and $F_3(\omega_0)$ (circles), as a function of $\omega_0 T/2\pi$ for the device with pressure $p = 10^{-1}$. For all data, $\omega_0 = 14.9$, $A_0 = 10^{-6}$, $b = 10^{-3}$, and the sampling time $\omega_0 \Delta/2\pi = 5.9 \times 10^{-3}$.

FIG. 21. The gain $G(\omega_0)$ for the acoustic device as a function of pressure p (for a system with no contact breaking) measured with sampling interval $\omega_0 \Delta/2\pi = 4.7 \times 10^{-2}$ (circles), 2.4×10^{-2} (Xs), 5.8×10^{-3} (triangles), and 2.9×10^{-3} (squares). The inset shows the Fourier transforms of the output and input signals, $F_1(\omega_0)$ (Xs) and $F_3(\omega_0)$ (circles), as a function of $\omega_0 \Delta/2\pi$ for the device with pressure $p = 10^{-1}$. For all data, $\omega_0 = 14.9$, $A_0 = 10^{-6}$, $b = 10^{-3}$, and the total simulation time $\omega_0 T/2\pi = 5.9 \times 10^4$.

FIG. 23. The ratio of the gain $G_{\mathrm{on}}(\omega_0)/G_{\mathrm{off}}(\omega_0)$ in the on state to that in the off state as a function of the normalized difference in pressure $(p_{\mathrm{on}} - p_{\mathrm{off}})/p_{\mathrm{on}}$ between the on and off states for mass ratios $m_L/m_S = 10$ (circles), 3 (Xs), and 1 (triangles). The devices are driven at the frequencies ω_0 indicated by the dashed lines in Figs. 22(a)–22(c).
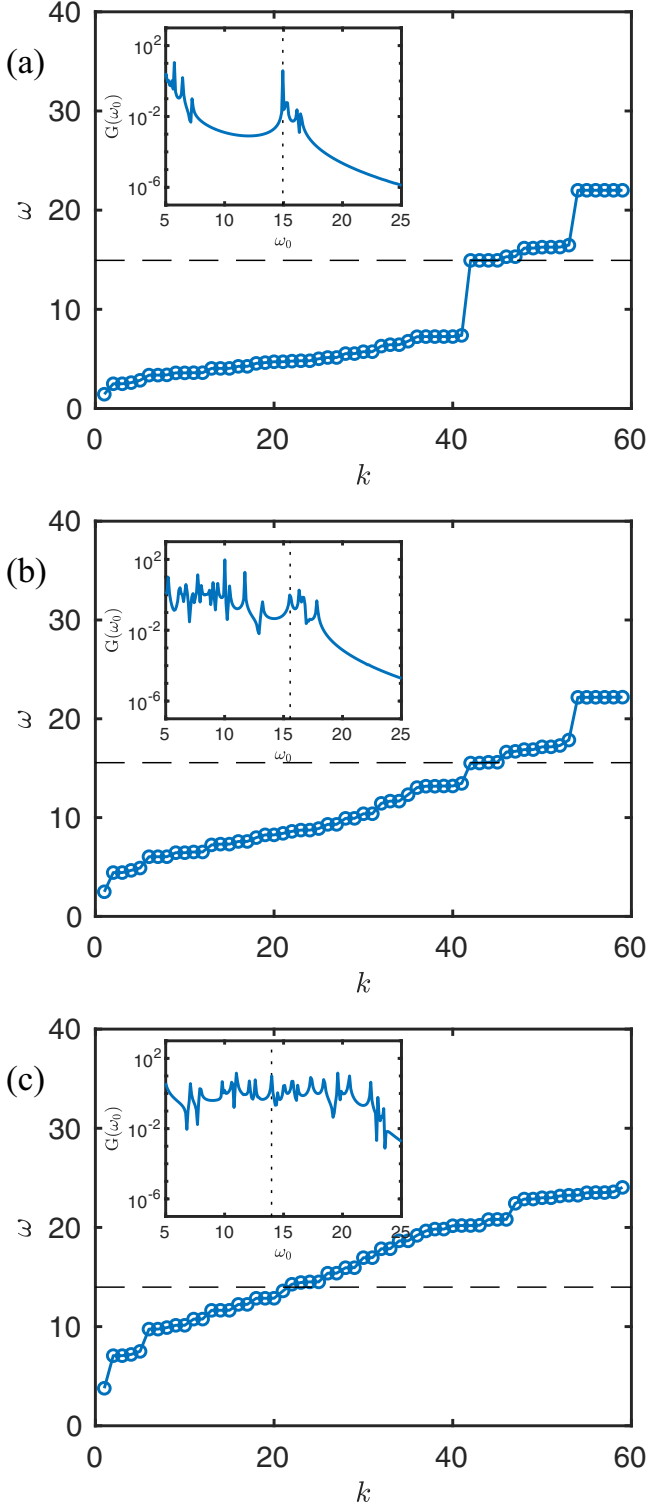

FIG. 22. Spectrum of eigenfrequencies for the mass-weighted dynamical matrix for the hexagonal lattice in the inset to Fig. 4 with $N_L = 21$ and $N_S = 9$ for mass ratios (a) $m_L/m_S = 10$, (b) 3, and (c) 1. The horizontal dashed lines indicate the frequencies at which we seek to drive the acoustic switching device. The insets of each panel show the frequency-dependent gain $G(\omega_0)$ (ratio of the Fourier transforms of the output and input signals) for the respective mass ratios. For all systems, the pressure $p = 10^{-1}$.
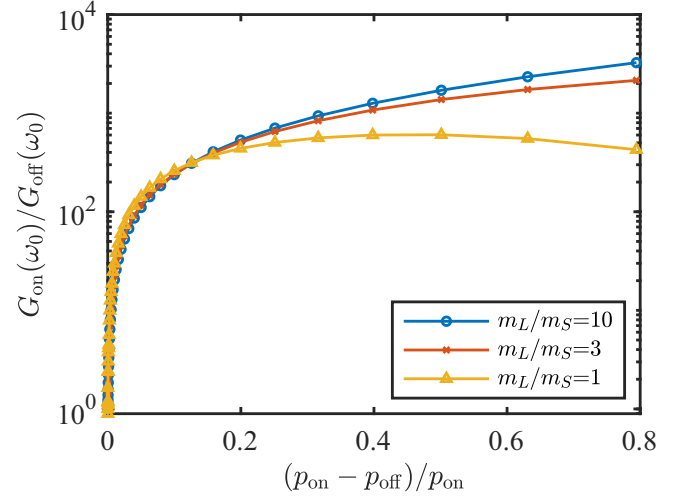
In the inset to Fig. 20, we show the Fourier transforms for the output and input signals, $F_1(\omega_0)$ and $F_3(\omega_0)$, as a function of the total time $\omega_0 T/2\pi$ when the system in the inset to Fig. 4 with $N = 30$ is driven at frequency $\omega_0 = 14.9$ and amplitude $A_0 = 10^{-6}$. We find only weak dependence of the Fourier transform on the total time in the range $\omega_0 T/2\pi \gtrsim 10^{4.5}$. In the main panel of Fig. 20, we show that the gain $G(\omega_0)$ versus pressure p is nearly identical for $\omega_0 T/2\pi = 10^4$ and 10^5. Thus, we selected $\omega_0 T/2\pi = 5.9 \times 10^4$ to calculate all of the discrete Fourier transforms. In the inset to Fig. 21, we show the dependence of the Fourier transforms $F_1(\omega_0)$ and $F_3(\omega_0)$ on the sampling time $\omega_0 \Delta/2\pi$. For $\omega_0 \Delta/2\pi \lesssim 10^{-2}$, $F_1(\omega_0)$ and $F_3(\omega_0)$ do not depend strongly on the sampling time. In the main panel of Fig. 21, we show that for most pressures the gain $G(\omega_0)$ does not depend on Δ. However, at pressures for which there is large gain, we find that we need to use $\omega_0 \Delta/2\pi \leqslant 5.8 \times 10^{-3}$ to reach convergence. Thus, we used this value of Δ to calculate all of the discrete Fourier transforms.

APPENDIX B: PERFORMANCE OF ACOUSTIC SWITCHING DEVICES WITH SMALL BAND GAPS

In the main text, we described acoustic switching devices that possess large frequency band gaps in their vibrational density of states. However, we have not yet discussed how the performance of the devices change with the size of the band gap. In Fig. 22, we show the eigenfrequency spectrum of the mass-weighted dynamical matrix for three mass ratios, $m_L/m_S = 10$, 3, and 1. As shown previously in Fig. 4, the maximum difference between adjacent eigenfrequencies w decreases as $m_L/m_S \to 1$. When there is a large band gap, we expect that we can generate a well-defined on state by driving the system at an eigenfrequency that populates the vibrational density of states. In addition, we expect that we can create

a well-defined off state, e.g., by decreasing the pressure of the system (which increases all of the eigenfrequencies) so that the driving frequency now occurs within the band gap. (See the difference between the Xs and circles in Fig. 7.) The frequency-dependent gain (ratio of the Fourier transforms of the output to the input signal) for a system with a large band gap is shown in the inset to Fig. 22(a). Indeed, the gain at $\omega = 14.9$ is ≈ 10, while the gain at nearby *lower* frequencies is several orders of magnitude lower. Thus, it is clear that an acoustic switch can be created by choosing the on state as the system with reference pressure ($p = 10^{-1}$) in Fig. 22(a) driven at frequency $\omega_0 = 14.9$ and choosing the pressure for the off state so that $G(\omega_0) \lesssim 10^{-2}$. Similar behavior is shown in Fig. 22(b) for a system with a smaller band gap at mass ratio $m_L/m_S = 3$. For example, the on state can be generated by driving the system at $\omega_0 = 15.5$, where the gain possesses a peak. The gain at nearby lower frequencies is smaller, but the gain has another peak at $\omega_0 = 13.2$. Thus, the operating range of the pressure difference of the acoustic switch decreases as the band gap decreases.

We now focus on the continuous eigenfrequency regime near $\omega_0 = 14.0$ for systems with $m_L/m_S = 1$ in Fig. 22(c). The frequency-dependent gain possesses a peak at $\omega_0 = 14.0$,

but the next peak in $G(\omega_0)$ at lower frequency does not occur until $\omega_0 = 12.6$, even though the eigenfrequency spectrum includes three eigenfrequencies between 12.6 and 14.0. For these eigenfrequencies, the overlap between the eigenmodes and either the input or output signal is small, and thus the output signal is weak when the system is driven at these eigenfrequencies. As a result, the gain ratio can be large even for systems with a continuous eigenfrequency spectrum. In Fig. 23, we show that the device with $m_L/m_S = 1$ can achieve a gain ratio $G_{\mathrm{on}}(\omega_0)/G_{\mathrm{off}}(\omega_0) > 10^2$.

Thus, we have shown that the vibrational response of the device at a given eigenfrequency depends on the overlap between the eigenmodes near the driving frequency and the input and output signals. A robust acoustic switch can always be produced using a system with a finite frequency band gap. However, an acoustic switch can also be created using a system with a continuous eigenfrequency spectrum if the driving frequency is chosen such that the eigenmodes of the corresponding nearby eigenfrequencies do not couple to the input and output signals. Such acoustic switching devices are more difficult to design since one needs to control the spatial structure of the eigenmodes, as well as the eigenfrequency spectrum.

[1] S. Alagoz, J. Acoust. Soc. Am. **133**, EL485 (2013).

[2] N. Boechler, G. Theocharis, and C. Daraio, Nat. Mater. **10**, 665 (2011).

[3] F. Li, P. Anzel, J. Yang, P. G. Kevrekidis, and C. Araio, Nat. Commun. **5**, 5311 (2014).

[4] G. Gantzounis, M. Serra-Garcia, K. Homma, J. M. Mendoza, and C. Daraio, J. Appl. Phys. **114**, 093514 (2013).

[5] L. Zigoneanu, B.-I. Popa, and S. A. Cummer, Nat. Mater. **13**, 352 (2014).

[6] S. A. Cummer, Science **343**, 495 (2014).

[7] E. B. Herbold, J. Kim, V. F. Nesterenko, S. Y. Wang, and C. Daraio, Acta Mech. **205**, 85 (2009).

[8] N. Boechler, J. Yang, G. Theocharis, P. G. Kevrekidis, and C. Daraio, J. Appl. Phys. **109**, 074906 (2011).

[9] A. Sokolow, E. G. Bittle, and S. Sen, Europhys. Lett. **77**, 24002 (2007).

[10] V. F. Nesterenko, J. Appl. Mech. Tech. Phys. (USSR) **24**, 733 (1983).

[11] C. F. Schreck, C. S. O'Hern, and M. D. Shattuck, Granul. Matter **16**, 209 (2014).

[12] J. Bardeen and W. H. Brattain, Phys. Rev. **74**, 230 (1948).

[13] F. Göncü, S. Luding, and K. Bertoldi, J. Acoust. Soc. Am. **131**, EL475 (2012).

[14] F. Göncü, S. Willshaw, J. Shim, J. Cusack, S. Luding, T. Mullin, and K. Bertoldi, Soft Matter **7**, 2321 (2011).

[15] V. Tournat, V. Zaitsev, V. Gusev, V. Nazarov, P. Béquin, and B. Castagnéde, Phys. Rev. Lett. **92**, 085502 (2004).

[16] C. F. Schreck, T. Bertrand, C. S. O'Hern, and M. D. Shattuck, Phys. Rev. Lett. **107**, 078301 (2011).

[17] M. Saadatfar, H. Takeuchi, V. Robins, N. Francois, and Y. Hiraoka, Nat. Commun. **8**, 15082 (2017).

[18] F. Rietz, C. Radin, H. L. Swinney, and M. Schröter, Phys. Rev. Lett. **120**, 055701 (2018).

[19] A. Tanguy, J. P. Wittmer, F. Leonforte, and J.-L. Barrat, Phys. Rev. B **66**, 174205 (2002).

[20] T. Bertrand, C. F. Schreck, C. S. O'Hern, and M. D. Shattuck, Phys. Rev. E **89**, 062203 (2014).

[21] Q. Wu, T. Bertrand, M. D. Shattuck, and C. S. O'Hern, Phys. Rev. E **96**, 062902 (2017).

[22] P. M. Reis, R. A. Ingale, and M. D. Shattuck, Phys. Rev. Lett. **96**, 258001 (2006).

[23] A. Panaitescu, K. A. Reddy, and A. Kudrolli, Phys. Rev. Lett. **108**, 108001 (2012).

[24] K. E. Daniels and R. P. Behringer, Phys. Rev. Lett. **94**, 168001 (2005).

[25] E. Ben-Naim, J. B. Knight, E. R. Nowak, H. M. Jaeger, and S. R. Nagel, Physica D **123**, 380 (1998).

[26] J. M. N. T. Gray, Ann. Rev. Fluid Mech. **50**, 407 (2018).

[27] K. M. Hill, D. V. Khakar, J. F. Gilchrist, J. J. MacCarthy, and J. M. Ottino, Proc. Natl. Acad. Sci. USA **96**, 11701 (1999).

[28] M. Souaille and B. Roux, Comput. Phys. Commun. **135**, 40 (2001).

[29] M. A. Gonzalez, E. Sanz, C. McBride, J. L. F. Abascal, C. Vega, and C. Valeriani, Phys. Chem. Chem. Phys. **16**, 24913 (2014).

[30] M. Mezei, Mol. Simul. **3**, 301 (1989).

[31] Y. Huang and S.-T. Ho, Opt. Express **16**, 16806 (2008).